Determining the transfer function of a reconstructive spectrometer using measurements at two wavelengths

Sharma, Naresh; Khare, Kedar; Gupta, Shilpi

DOI
10.1364/OL.494412

Publication date
2023

Document Version
Final published version

Published in
Optics Letters

Optics Letters

Determining the transfer function of a reconstructive spectrometer using measurements at two wavelengths

Naresh Sharma,[1] Kedar Khare,[2] and Shilpi Gupta[3,4,*]

[1]Optics Research Group, ImPhys Department, Faculty of Applied Sciences, Delft University of Technology, Delft 2628 CJ, The Netherlands
[2]Optics and Photonics Centre, Indian Institute of Technology Delhi, New Delhi-110016, New Delhi, India
[3]Department of Electrical Engineering, Indian Institute of Technology Kanpur, Kanpur-208016, UP, India
[4]Centre for Lasers and Photonics, Indian Institute of Technology Kanpur, Kanpur-208016, UP, India
*ShilpiG@iitk.ac.in

Received 10 May 2023; revised 15 June 2023; accepted 15 June 2023; posted 15 June 2023; published 10 July 2023

The transfer function is the characteristic function of the dispersive element of a reconstructive spectrometer. It maps the transmitted spatial intensity profile to the incident spectral intensity profile of an input. Typically, a widely tunable and narrowband source is required to determine the transfer function across the entire operating wavelength range, which increases the developmental cost of these reconstructive spectrometers. In this Letter, we utilize the parabolic dispersion relation of a planar one-dimensional photonic crystal cavity, which acts as the dispersive element, to determine the entire transfer function of the spectrometer using measurements made at only two wavelengths. Using this approach, we demonstrate reliable reconstruction of input spectra in simulations, even in the presence of noise. The experimentally reconstructed spectra also follow the spectra measured using a commercial spectrometer.

https://doi.org/10.1364/OL.494412

Introduction. Reconstructive spectrometers recover an input frequency spectrum by solving an inverse problem using different computational algorithms [1–9]. These compact spectrometers offer high resolution and break the inevitable size-resolution trade-off of conventional spectrometers. Their operating principle relies on mapping the spatial information to the spectral information using the transfer function of the system, which is the pre-calibrated system response. Different platforms such as patterned photonic crystals [10–12], disordered photonic structures [2], photonic crystal cavities [1,13,14], miniaturized microdonut resonators [15], integrated micro-ring resonator with diffraction gratings [16], arrayed waveguide gratings [17], variable material absorption [18], spectral filters [19,20], surface plasmon polaritons [21], and dielectric metasurfaces [22], have been used to demonstrate reconstructive spectrometers. Prior to our recent work [1], most of these demonstrations relied on complex and expensive fabrication techniques and were sensitive to optical misalignment. Our demonstration utilized a scalable fabrication technique, a low-cost web camera, and a computational reconstruction technique to reliably reconstruct the input spectrum in the presence of noise and optical misalignment.

A critical issue that remains unaddressed by the state-of-the-art reconstructive spectrometers, including our recent work [1], is the requirement of a tunable and narrowband source to generate the transfer function of the system for use in the reconstruction algorithm. This requirement increases the cost of development of the spectrometer and hinders wide deployment in the field. Here, we propose and demonstrate a technique that eliminates the need of a tunable and narrowband source to generate the transfer function of a reconstructive spectrometer based on a planar one-dimensional photonic crystal cavity. The technique utilizes the parabolic dispersion relation of the cavity that can be characterized over the entire operating wavelength range by measurements made at only two wavelengths. Through finite-difference time-domain (FDTD) simulations, we show that the technique reliably reconstructs the input spectra, even in the presence of noise. We also experimentally reconstruct the input spectra and compare them with the spectra measured using a commercial spectrometer.

Theoretical modeling. *System description.* The reconstructive spectrometer is comprised of an objective lens, a planar one-dimensional photonic crystal cavity, a screen, and a web-camera [1]. When an input beam is focused on the photonic crystal cavity using the objective lens, the transmitted beam is comprised of annular beams of different divergence angles corresponding to different wavelengths present in the input spectrum (Fig. 1). The transmitted beams have annular spatial profiles because the photonic crystal cavity acts as a resonant spatial filter. An incident wavelength needs to be shorter than the cavity resonance wavelength at normal incidence to generate an annular beam in transmission [23].

FDTD simulations. We focus a linearly (vertically) polarized laser source using an objective lens (numerical aperture, NA = 0.9) on the one-dimensional photonic crystal cavity (Fig. 1) [1,23]. A focused beam has different polarization directions for different parts of the beam. When the input to the objective lens is a vertically polarized and collimated beam, the polarization of

Corrected 13 July 2023

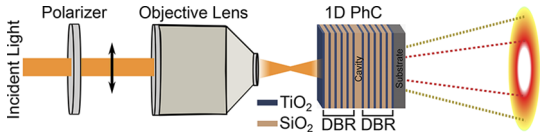

Fig. 1. Schematic of a reconstructive spectrometer based on a one-dimensional photonic crystal cavity (1D PhC): DBR, distributed Bragg reflector.

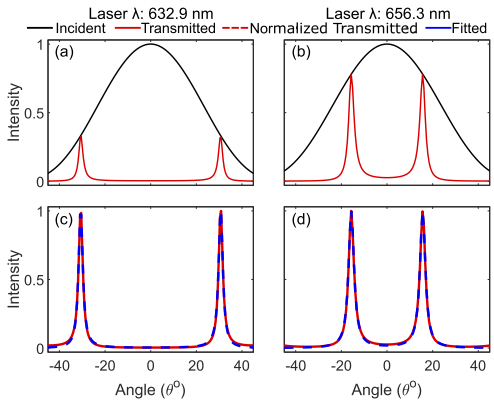

Fig. 2. (a),(b) Simulated intensity as a function of divergence angle: incident on (black solid curves) and transmitted by (red solid curves) a photonic crystal cavity. The incident laser wavelengths are 632.9 nm and 656.3 nm. (c),(d) Normalized transmitted intensity profiles (red dashed curves) for both the laser wavelengths and the associated Lorentzian fits (blue dashed curves).

the focused beam after the objective lens is transverse magnetic (TM) in the vertical direction and transverse electric (TE) in the horizontal direction [23].

We calculate the transmitted intensity profile as a function of the divergence angle (θ) for a fixed azimuthal angle ($\phi = 90°$ representing TM polarization) using the FDTD method (Lumerical Inc) (Fig. 2). While both TM and TE polarizations are present in the transmitted beam, we work with only TM polarization because the transmitted annular beam has higher intensity for the TM polarization (vertical direction) than the TE polarization (horizontal direction) due to the polarization-dependent transmission coefficient [1,23]. The positive and negative angles ($+\theta$ and $-\theta$) correspond to azimuthal angles differing by 180°. The planar symmetry of the photonic crystal cavity translates into symmetry in the transmitted intensity profile in the transverse plane. The black solid curves in Figs. 2(a) and 2(b) show the intensity profiles of linearly polarized laser beams (at wavelengths 632.9 nm and 656.3 nm) incident on the photonic crystal cavity as a function of divergence angle for TM polarization [23]. The incident intensity profiles follow a Gaussian distribution with width decided by the NA of the objective lens. Both the laser wavelengths are shorter than the cavity resonance wavelength (670 nm), and therefore, the cavity transmits a narrow band of angles at the incident wavelengths [red curves in Figs. 2(a) and 2(b)], resulting in annular spatial profiles of the transmitted beam.

We observe the amplitude and the angular location of the peak of the transmitted intensity depend on the incident laser wavelength. The closer the incident wavelength is to the cavity resonance wavelength at normal incidence, the smaller the divergence angle of the transmitted annular beam is. Since the divergence angle is imparted by the objective lens, the peak amplitude of the transmitted beam is decided by the NA of the objective lens. We normalize the transmitted profiles to the incident intensity profiles [red dotted curves in Figs. 2(c) and 2(d)]. This normalization removes the wavelength-dependent amplitude variation in the transmitted intensity profiles which is introduced by the objective lens. These normalized transmitted profiles are essentially the transfer function of the photonic crystal cavity at the specific incident wavelengths. We fit both of these normalized transmitted intensity profiles to a Lorentzian function [Figs. 2(c) and 2(d), blue dotted curves], and find that the Lorentzian function is indeed a good fit. These transmitted intensity profiles peak at a resonance angle (θ_i) that is a function of the difference in the incident wavelength (λ_i) and the cavity resonance wavelength (λ_c) and have a full width at half maximum (FWHM) of $\delta\theta_i$. Therefore, we model the transfer function of the photonic crystal cavity, $T(\theta_i, \lambda_i)$, at incident wavelength λ_i as a Lorentzian function centered at resonance angle θ_i with a FWHM of $\delta\theta_i$ and the peak amplitude set to unity.

Next, we calculate the transfer function matrix across the entire operating wavelength range of the spectrometer by determining the resonance angle and the FWHM of the resonance as a function of the incident wavelength using only two laser sources. We calculate the resonance angle of the one-dimensional planar photonic crystal cavity as a function of the incident wavelength by the following analytical expression [1]:

$$\omega_i = Ak_o^2 \sin^2\theta_i + \omega_c, \tag{1}$$

where $\omega_c{=}2\pi c/\lambda_c$, $\omega_i{=}2\pi c/\lambda_i$, $k_0{=}2\pi/\lambda_i$, and A is a constant which depends on the design parameters of the system. We determine resonance angles for two available laser wavelengths by capturing their transmitted annular intensity profiles at two positions separated by 33 mm along the direction normal to the photonic crystal structure (Supplementary figure S1). Using these two resonance angles, we determine the two unknown parameters, A and λ_c, of Eq. (1) and fully characterize the $\lambda_i - \theta_i$ relation. This calculated $\lambda_i - \theta_i$ relation matches well with the results calculated using FDTD method by varying the incident wavelength (Supplementary figure S2a). Similarly, we determine the FWHM of the resonances of the two laser wavelengths from the widths of the transmitted annular intensity profiles [1] and fully characterize the $\lambda_i - \delta\theta_i$ relation (details in the Supplement 1). Using the resonance angles, we also calculate the location of the waist of the beam focused by the objective lens (Supplementary figure S1). Figure 3(a) shows the transfer function [$T(\theta, \lambda)$] of the photonic crystal cavity calculated using only two laser sources (wavelengths 632.9 nm and 656.3 nm) that are TM polarized. Our calculated transfer function matches well with the transfer function calculated using the FDTD method by varying the incident wavelength [Supplementary figures S2(b) and S2(c)].

Finally, we use the calculated transfer function to reconstruct spectra of two different inputs (Table 1). First, we capture the transmitted spatial intensity profiles of the two inputs after passing through the photonic crystal cavity [Figs. 3(b) and 3(c)]. Since the location of the beam waist is already known, we capture the transmitted intensity profiles for both the input spectra at only one position and calculate the transmitted intensity profiles as a function of divergence angle for both the input spectra (Supplementary figure S1). We assume that all input beams fill the aperture of the objective lens so that the angle-dependent intensity variation is decided by only the NA of the objective

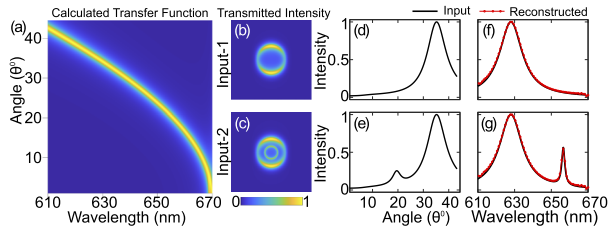

Fig. 3. (a) Theoretically calculated transfer function, $T(\theta, \lambda)$, as a function of angle and input wavelength for TM polarization direction using only two laser sources. (b),(c) Transmitted intensity profiles of the two inputs. (d),(e) Normalized transmitted intensity profiles $[I(\theta)]$ as a function of angle of the two inputs. (f),(g) Incident (black curves) and reconstructed spectra (red curves) of the two inputs.

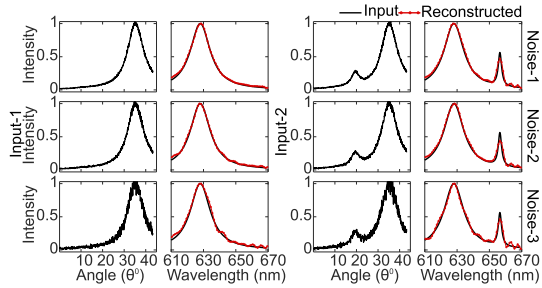

Fig. 4. Simulated incident (black curves) and reconstructed spectra (red curves) for the two inputs in presence of three noise levels. Noise-1, Noise-2, and Noise-3 represent 1000, 500, and 100 photons per pixel, respectively.

Table 1. Parameters of Input Spectra

Input	Profile	Peak Wavelength	FWHM	Amplitude
1	One Lorentzian	628 nm	15 nm	1
2	Two Lorentzian	628 nm	15 nm	1
		656.3 nm	2 nm	0.5

lens and the wavelength of the input source. We model the angle-dependent intensity profile of any input beam after the objective lens as a Gaussian distribution with its FWHM equal to an average of the FWHMs measured for the two calibrating laser sources (632.9 nm and 656.3 nm). This approximation eliminates the need of removing the photonic crystal cavity to measure the angle-dependent intensity profile of each input after the objective lens for normalization purposes. Figures 3(d) and 3(e) show the transmitted spatial intensity profiles $[I(\theta)]$ of the two inputs as a function of the divergence angle, normalized with respect to the Gaussian distribution that represents the angle-dependent intensity profile after the objective lens. The transfer function of the photonic crystal cavity $[T(\theta, \lambda)]$ relates the transmitted spatial intensity profile $[I(\theta)]$ to the incident spectral intensity profile $[I(\lambda)]$ using the following expression [1]:

$$I(\theta) = \sum_{i=1}^{N} T(\theta, \lambda_n) I(\lambda_i). \quad (2)$$

Using Eq. (2), we reconstruct both the spectra [Figs. 3(f) and 3(g)] that follow the input spectra (black curve) set in the simulation well. Our technique measures the peak wavelengths of the input spectra as 627.88 ± 0.09 nm and 656.33 ± 0.06 nm.

Generally, the solution of an inverse problem is sensitive to inevitable measurement errors and instrument noise. Therefore, to check the robustness of our reconstruction technique in simulations, we reconstruct the spectrum in the presence of noise. We deliberately add Poisson noise in I(θ) using the following expression:

$$I(\theta) = Poisson\left(I(\theta)\frac{N_{ph}}{\overline{I(\theta)}}\right), \quad (3)$$

where *Poisson* generates random numbers from the Poisson distribution and N_{ph} is the average number of photons per pixel incident on the detector. We use the mean gradient descent (MGD) method with an L2-norm squared error as a data fitting term and the Huber penalty as a regularizer to find the optimized reconstructed spectrum [24]. As an initial guess, we use truncated singular value decomposition to eliminate some part of the transmitted intensity $I(\theta)$ which is most easily affected by the noise. We reconstruct spectra of both the inputs for three different values of noise levels: 1000; 500; and 100 photons per pixel (Fig. 4). Our method is able to reconstruct the spectrum for 100 photons per pixels, which is an acceptable noise level for practical situations. We observe a slightly lower amplitude of the narrower peak (at 656.3 nm) in Input-2 after reconstruction in comparison with the input spectrum. We attribute this amplitude difference to the regularization process used in our reconstruction algorithm, which is required to minimize grainy artefacts in the reconstructed spectrum.

Experiment. We fabricate a photonic crystal cavity by introducing a silicon dioxide (SiO_2) defect between two distributed Bragg reflectors, each composed of six alternate thin films of SiO_2 and titanium dioxide (TiO_2) [1,23]. We focus a vertically polarized and collimated laser beam (details in the Supplement 1) on the photonic crystal cavity using an objective (NA: 0.9) lens (Supplementary figure S1). We measure the intensity profiles, incident on the cavity and transmitted by the cavity, at two positions separated by 33 mm along the normal direction of the photonic crystal structure for laser wavelengths 632.9 nm and 656.3 nm (Supplementary figure S3).

We observe that the incident intensity profiles follow a Gaussian distribution centered at 0° angle and the transmitted intensity profiles follow a Lorentzian distribution centered at the resonance angle (Supplementary figure S3), both for TM polarization. By normalizing the transmitted intensity profiles with the incident intensity profiles, we calculate the resonance angles (resonance widths) for laser wavelengths λ_1 = 632.9 nm and λ_2 = 656.3 nm as 29.77°(2.49°) and 17.68°(3.40°) for TM polarization. Following the same procedure as in simulation, we calculate the transfer function [Fig. 5(a)] using Eq. (1), and resonance angles and resonance widths of the two laser sources.

Finally, we test our technique to experimentally reconstruct two different input spectra (Table 1). We capture the transmitted intensity profiles for both the input spectra at a single position only [Figs. 5(b) and 5(c)]. We follow the same procedure as discussed in the simulations section and normalize the transmitted intensity to the incident intensity profiles. Figures 5(d) and 5(e) show the normalized transmitted intensity profiles as a function of divergence angle obtained by removing the angle-dependent variation introduced by the objective lens. Using these normalized transmitted intensity profiles [Figs. 5(d) and 5(e)], the calculated transfer function [Fig. 5(a)], Eq. (2), and the mean

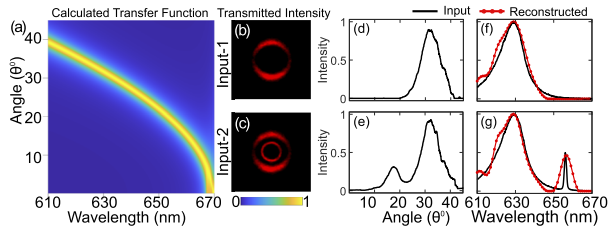

Fig. 5. (a) Experimentally calculated transfer function $T(\theta, \lambda)$ as a function of angle and input wavelength for the fabricated sample using the two laser sources. (b),(c) Experimentally measured transmitted intensity profiles of the two inputs. (d),(e) Normalized transmitted intensity profiles [I(θ)] as a function of angle for the two inputs. (f),(g) Incident (black curves) and reconstructed spectra (red curves) of the two inputs. The incident spectra are measured using a fiber-based spectrometer (HR4000 Ocean Optics). All scale bars are 10 mm. All images of the transmitted beam are adjusted to the same maximum brightness and the same contrast enhancement.

gradient descent method, we reconstruct the input spectra [red curves in Figs. 5(f) and 5(g)] which follow the spectra measured using a commercial spectrometer with a resolution of 1 nm [black curves in Figs. 5(f) and 5(g)]. The absolute relative error in the peak wavelengths of the reconstructed spectra is less than 1 nm. We observe little bumps in the reconstructed spectra due to background noise, which can be suppressed by increasing the noise tolerance in the reconstruction algorithm. We also observe the width of the narrower peak in Input-2 in the reconstructed spectrum is broader than in the spectrum measured using the commercial spectrometer. We attribute this difference in the reconstructed and the input spectra to the cavity linewidth ($\approx$ 5 nm at normal incidence; Supplementary figure S4) of our structure. To confirm this, we reconstruct a narrowband laser spectrum (Supplementary figure S5) and observe that the minimum linewidth of the reconstructed spectrum is limited by the cavity linewidth of the structure. The cavity linewidth of the structure can be reduced by increasing the number of periodic layers [25–27], which will aid in an accurate reconstruction of the input spectrum.

Conclusion and discussion. In conclusion, we have proposed and experimentally demonstrated a technique to determine the transfer function of a reconstructive spectrometer, across the entire operating wavelength range, by making measurements at only two wavelengths. Our technique utilizes the parabolic dispersion relation of a planar one-dimensional photonic crystal cavity. The transfer function calculated using only two laser sources matches well with the transfer function calculated using finite difference time domain simulations. This technique eliminates the requirement of a widely tunable and narrowband light source for calibration of the spectrometer. We have experimentally compared the spectrum reconstructed using our technique with the spectrum measured using a commercial spectrometer. The spectral resolution of the spectrometer depends on the cavity linewidth and can be improved by increasing the number of periodic layers in the distributed Bragg reflectors. While the initial calibration of the spectrometer requires measurements at two positions along the optics axis of the system, reconstruction of an unknown input requires measurement at only one position, eliminating movement of any component and adding to the stability of the system. Our proposed technique can be easily applied to any reconstructive spectrometer whose dispersive element exhibits a parabolic dispersion relation, irrespective of the fabrication method or material choice.

Funding. Department of Science and Technology, Ministry of Science and Technology, India (SR/FST/ETII- 265 072/2016); Science and Engineering Research Board (CRG/2021/003265); Indian National Academy of Engineering.

Acknowledgments. We thank R. Vijaya and Govind Kumar for fabrication support. This work was supported through Kedar Khare's Abdul Kalam Technology Innovation National Fellowship.

Disclosures. The authors declare no conflicts of interest.

Data availability. Raw data and codes underlying the results presented in this paper are not publicly available at this time but may be obtained from the authors upon reasonable request.

Supplemental document. See Supplement 1 for supporting content.

REFERENCES

1. N. Sharma, G. Kumar, V. Garg, R. G. Mote, and S. Gupta, Opt. Express **29**, 26645 (2021).
2. B. Redding, S. F. Liew, R. Sarma, and H. Cao, Nat. Photonics **7**, 746 (2013).
3. C.-C. Chang and H.-N. Lee, Opt. Express **16**, 1056 (2008).
4. S. Zhang, Y. Dong, H. Fu, S.-L. Huang, and L. Zhang, Sensors **18**, 644 (2018).
5. T. Yang, C. Li, Z. Wang, and H. Ho, Optik **124**, 1377 (2013).
6. U. Kurokawa, B. I. Choi, and C.-C. Chang, IEEE Sens. J. **11**, 1556 (2011).
7. C.-C. Chang and H.-Y. Lin, IEEE Sens. J. **12**, 2586 (2012).
8. P. Wang and R. Menon, Opt. Express **22**, 14575 (2014).
9. J. Oliver, W. Lee, S. Park, and H.-N. Lee, Opt. Express **20**, 2613 (2012).
10. N. K. Pervez, W. Cheng, Z. Jia, M. P. Cox, H. M. Edrees, and I. Kymissis, Opt. Express **18**, 8277 (2010).
11. Z. Wang, S. Yi, A. Chen, M. Zhou, T. S. Luk, A. James, J. Nogan, W. Ross, G. Joe, A. Shahsafi, K. X. Wang, M. A. Kats, and Zongfu Yu, Nat. Commun. **10**, 1020 (2019).
12. K. M. Bryan, Z. Jia, N. K. Pervez, M. P. Cox, M. J. Gazes, and I. Kymissis, Opt. Express **21**, 4411 (2013).
13. X. Gan, N. Pervez, I. Kymissis, F. Hatami, and D. Englund, Appl. Phys. Lett. **100**, 231104 (2012).
14. F. Meng, R.-J. Shiue, N. Wan, L. Li, J. Nie, N. C. Harris, E. H. Chen, T. Schröder, N. Pervez, I. Kymissis, and D. Englund, Appl. Phys. Lett. **105**, 051103 (2014).
15. Z. Xia, A. A. Eftekhar, M. Soltani, B. Momeni, Q. Li, M. Chamanzar, S. Yegnanarayanan, and A. Adibi, Opt. Express **19**, 12356 (2011).
16. B. B. Kyotoku, L. Chen, and M. Lipson, Opt. Express **18**, 102 (2010).
17. P. Cheben, J. Schmid, A. Delâge, A. Densmore, S. Janz, B. Lamontagne, J. Lapointe, E. Post, P. Waldron, and D.-X. Xu, Opt. Express **15**, 2299 (2007).
18. Y. Maruyama, K. Sawada, H. Takao, and M. Ishida, IEEE Trans. Electron Devices **53**, 553 (2006).
19. J. Bao and M. G. Bawendi, Nature **523**, 67 (2015).
20. S.-W. Wang, C. Xia, X. Chen, W. Lu, M. Li, H. Wang, W. Zheng, and T. Zhang, Opt. Lett. **32**, 632 (2007).
21. Y. Tsur and A. Arie, Opt. Lett. **41**, 3523 (2016).
22. M. Faraji-Dana, E. Arbabi, A. Arbabi, S. M. Kamali, H. Kwon, and A. Faraon, Nat. Commun. **9**, 4196 (2018).
23. N. Sharma, G. Kumar, V. Garg, R. G. Mote, V. Ramarao, and S. Gupta, IEEE Photonics Technol. Lett. **32**, 1273 (2020).
24. S. Rajora, M. Butola, and K. Khare, Appl. Opt. **60**, 5669 (2021).
25. F. Réveret, L. Bignet, W. Zhigang, X. Lafosse, G. Patriarche, P. Disseix, F. Médard, M. Mihailovic, J. Leymarie, J. Zú niga-Pérez, and S. Bouchoule, J. Appl. Phys. **120**, 093107 (2016).
26. H. Knopf, N. Lundt, and T. Bucher, *et al.*, Opt. Mater. Express **9**, 598 (2019).

27. M. Anni, G. Gigli, R. Cingolani, S. Patane, A. Arena, and M. Allegrini, Appl. Phys. Lett. **79**, 1381 (2001).